



OPEN

Unchanged right ventricular strain in repaired tetralogy of Fallot after pulmonary valve replacement with radial long-axis cine magnetic resonance images

Masateru Kawakubo^{1✉}, Yuzo Yamasaki², Daisuke Toyomura³, Kenichiro Yamamura³, Ichiro Sakamoto⁴, Tetsuhiro Moriyama⁵, Hidetake Yabuuchi¹ & Kousei Ishigami²

We measured right ventricular (RV) strain by applying a novel postprocessing technique to conventional short-axis cine magnetic resonance imaging in the repaired tetralogy of Fallot (TOF) and investigated whether pulmonary valve replacement (PVR) changes the RV strain. Twenty-four patients with repaired TOF who underwent PVR and 16 healthy controls were enrolled. Global maximum and minimum principal strains (GPS_{max} , GPS_{min}) and global circumferential and longitudinal strains (GCS, GLS) were measured from short-axis cine images reconstructed radially along the long axis. Strain parameters before and after PVR were compared using paired t-tests. One-way ANOVA with Tukey post-hoc analysis was used for comparisons between the before and after PVR groups and the control group. There were no differences in strain parameters before and after PVR. The GPS_{max} before PVR was lower than that in the control group ($P = 0.002$). Before and after PVR, GCSs were higher and GLSs were lower than those in the control group (before and after GCSs: $P = 0.002$ for both, before and after GLSs: $P < 0.0001$ and $P = 0.0003$). RV strains from radially reconstructed short-axis cine images revealed unchanged myocardial motion after PVR. When compared to the control group, changes in GCS and GLS in TOF patients before and after PVR might be due to RV remodeling.

Patients with surgically repaired TOF experience significant morbidity and mortality related to biventricular dysfunction and arrhythmia in their adult years^{1–3}. These sequelae are believed to be in part related to chronic pulmonary regurgitation caused by efforts to relieve pulmonary valve stenosis with the initial repair. PVR is performed to improve pulmonary regurgitation or valvular stenosis and improve long-term outcomes^{4,5} in adult patients with repaired TOF. However, cardiovascular magnetic resonance (CMR) feature tracking showed that ventricular strain was unchanged, even after PVR⁶.

Peak strain is a helpful marker for quantifying myocardial tissue deformation^{7–9}, especially in the RV, because the image quality of echocardiography is sometimes inadequate^{10,11}. Generally, the RV strain is evaluated using circumferential strain (CS) or longitudinal strain (LS) from the motion of the endocardium in one plane of the ventricular short- or long-axis, respectively. However, the motion of the heart is three-dimensional. Accordingly, such predefined directions of change may not reliably describe deformation in the dominant direction of tissue movement established by engaged myocardial fibers. On the other hand, three-dimensional image acquisition for myocardial strain is technically difficult and time-consuming, if possible. Recently, the feasibility of three-dimensional image analysis using routine cine CMR images for the estimation of principal strain (PS), a geometry-independent measure established from the dominant direction of local tissue deformation, has been reported¹². Therefore, we measured RV PS of three-dimensional “real” strain in repaired TOF by applying this novel postprocessing technique to conventional two-dimensional cine imaging. In the present study, we

¹Department of Health Sciences, Faculty of Medical Sciences, Kyushu University, 3-1-1 Maidashi, Higashi-ku, Fukuoka-shi, Fukuoka 812-8582, Japan. ²Department of Clinical Radiology, Graduate School of Medical Sciences, Kyushu University, Fukuoka, Japan. ³Department of Pediatrics, Graduate School of Medical Sciences, Kyushu University, Fukuoka, Japan. ⁴Department of Cardiovascular Medicine, Kyushu University Hospital, Fukuoka, Japan. ⁵Institute of Mathematics for Industry, Kyushu University, Fukuoka, Japan. ✉email: kawakubo.masateru.968@m.kyushu-u.ac.jp

	TOF patients (n = 24)		P-value	Control (n = 16)
	Before PVR	After PVR		
Age before PVR (y)	26 ± 9			33 ± 11
Male/female	11/13			13/3
Body surface area before PVR (m ²)	1.58 ± 0.17			1.76 ± 0.13
WHO classification (I/II/III/IV)	17/5/2/0	23/1/0/0		16/0/0/0
CMR to PVR duration (day)	252 ± 158			
PVR to CMR duration (day)		433 ± 163		
CMR RV parameters				
HR (bpm)	70 ± 12	69 ± 9	0.41	66 ± 14
RVEDVi (mL/m ²)	165.7 ± 41.9	108.7 ± 19.0	<0.0001	71.0 ± 18.0
RVESVi (mL/m ²)	94.2 ± 29.7	66.0 ± 14.7	<0.0001	28.8 ± 10.9
RVEF (%)	43.8 ± 7.8	39.3 ± 7.1	0.02	60.5 ± 6.3
RVSVi (mL/m ²)	71.4 ± 19.5	42.7 ± 10.3	<0.0001	42.2 ± 8.1
Cardiac catheterization				
RVP (mmHg)	51.9 ± 18.8			
LVP (mmHg)	122.3 ± 17.0			
PA pressure (mmHg)	34.5 ± 12.0			
RVP/ LVP	0.43 ± 0.18			
RV-PA pressure gradient	17.4 ± 17.3			

Table 1. Baseline clinical characteristics, CMR right ventricular parameters, and right heart catheterization parameters. CMR cardiovascular magnetic resonance, EDVi indexed end-diastolic volume, EF ejection fraction, ESVi indexed end-systolic volume, HR heart rate, LVP left ventricular pressure, PA pulmonary artery, PVR pulmonary valve replacement, RV right ventricular, RVP right ventricular pressure, SVi stroke volume index, TOF tetralogy of Fallot, WHO World Health Organization. Significantly differences are expressed as bold P-values.

investigated whether PVR changes the RV PS. We also investigated the clinical impact of the relationship between strain parameters and clinical and hemodynamic measurements.

Results

Table 1 shows the baseline characteristics, CMR RV parameters, and cardiac catheterization parameters. After PVR, the World Health Organization class and RV volume parameters showed significant improvement.

Figure 1 shows the global strain parameters in the patients before and after PVR and in the control group. There were no differences in any of the strain parameters before and after PVR. The GPS_{max} before PVR was lower than that in the control group ($P = 0.002$). GCSs before and after PVR were higher than those in the control groups ($P = 0.002$ for both). GLSs before and after PVR were lower than those in the controls ($P < 0.0001$ and $P = 0.0003$). The r_s (confidence intervals) indicated significant correlations between the GPS_{min} and RVP/LVP ($r_s = -0.44 [-0.72, -0.03]$) and between the GPS_{min} and the RV-PA pressure gradient ($r_s = -0.54 [-0.78, -0.16]$) (Fig. 2). In addition, the GPS_{max} was significantly correlated with RVP/LVP and with the RV-PA pressure gradient ($r_s = 0.47 [0.08, 0.74]$, $r_s = 0.64 [0.31, 0.83]$) (Fig. 2).

There were strong correlations between intra- and inter-observer strains ($P < 0.01$). Excellent intra-observer and inter-observer reproducibility were observed for RV strain measurements using radial long-axis reconstructed cine images (Table 2).

Discussion

According to our investigation, there were no differences in global PS values before and after PVR in adult patients with surgically repaired TOF. Furthermore, GCS and GLS were unchanged before and after PVR. Our results are in line with those of previous research⁶. Therefore, PVR in patients with repaired TOF led to no changes in RV global PS. There were no differences in global PS between the patients after PVR and the control group, although the RV volume parameters were not normalized. This may indicate that RV myocardial motility is maintained by remodeling, corresponding to long-term pressure overloading. The mean RV ESVi in the patients before PVR was 94 mL/m², which corresponds to the previously reported adaptive RV remodeling conditions (73 to 113 mL/m²)¹³. Furthermore, in RV pressure overload, it is mainly the middle myocardial layer that hypertrophies^{14,15}. The RV in patients with adapted remodeling is similar to the normal left ventricle, which has a well-developed middle circumferential layer¹⁶. Thus, the increase in the circumferential fiber mass may also contribute to the predominant circumferential RV free-wall shortening. According to our results, increased GCS and decreased GLS in the TOF group relative to the control group were consistent with these reports. Furthermore, our results suggest that even if the RV volume is reduced by PVR, there is no reverse remodeling of myocardial motion 1 year after the surgery. Earlier surgical intervention might be preferable to prevent myocardial remodeling.

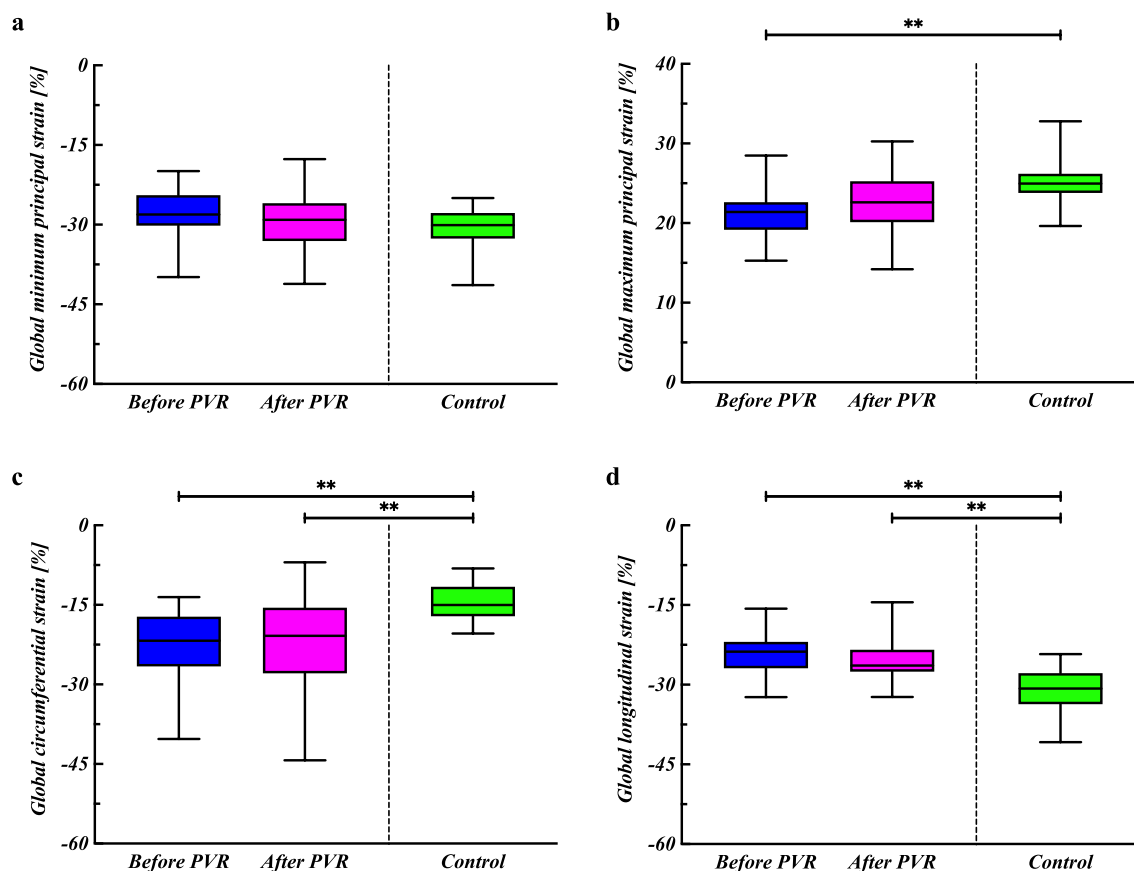


Figure 1. Global strain values of patients with tetralogy of Fallot before and after pulmonary valve replacement, and of control patients. The (a) global minimum principal strains, (b) global maximum principal strains, (c) global circumferential strains, and (d) global longitudinal strains are shown as box-and-whisker plots. ** $P < 0.01$, * $P < 0.05$.

In clinical situations, pressure parameters derived from cardiac catheterization are important indicators for PVR. We found that CMR-derived GPS_{min} and GPS_{max} were significantly correlated. The advantage of CMR with respect to cardiac catheterization is its accurate volume measurement and low invasiveness. However, its weakness is an inability to measure the pressure in the cardiac cavity or blood vessels. Surgical indications for PVR include volumetric parameters (e.g., RV dilatation) and pressure parameters (e.g., RVP/LVP). The estimation of pressure-derived parameters using our method has the potential to overcome CMR's weakness. Because our strain analysis requires only short-axis cine CMR, a well-established method without the need for additional imaging, a wider range of applications could be expected.

We acknowledge that our strain analysis with radially reconstructed long-axis cine CMR was based on the original in-house algorithm. Although measurements of RV PS with echocardiography using commercial software have been reported^{17,18}, no software has been established for RV PS for CMR. We considered that the values of PS, GCS, and GLS were clinically reasonable and reliable in the study populations. Furthermore, the reproducibility of the strain measurements with radially reconstructed long-axis images was compared with CMR-derived strain measurements using feature tracking^{19,20}. However, a future validation study by comparing the commercially available software with echocardiography would be required. Additionally, it will be necessary to verify the technique by applying the analysis to different right heart diseases and investigating their relationship with other clinical indicators and prognoses.

In this cohort, the three-dimensional PS revealed unchanged RV myocardial motion after PVR. In TOF patients before and after PVR, changes in GCS and GLS with respect to the control group might be due to RV remodeling. PS values reconstructed by short-axis CMR images were correlated with the parameters of pressure overloading with cardiac catheterization.

Methods

Patients. This retrospective observational study was approved by the institutional review board of Kyushu University and conducted in accordance with the 1964 Declaration of Helsinki. Written informed consent was obtained from each patient. Twenty-four patients with surgically repaired TOF who underwent PVR were enrolled in the study, and datasets derived between October 2012 and March 2018 were analyzed. All patients were older than 18 years and underwent CMR assessment and cardiac catheterization of the right and left heart before PVR. In addition, CMR control data were obtained from 16 age- and sex-matched healthy subjects.

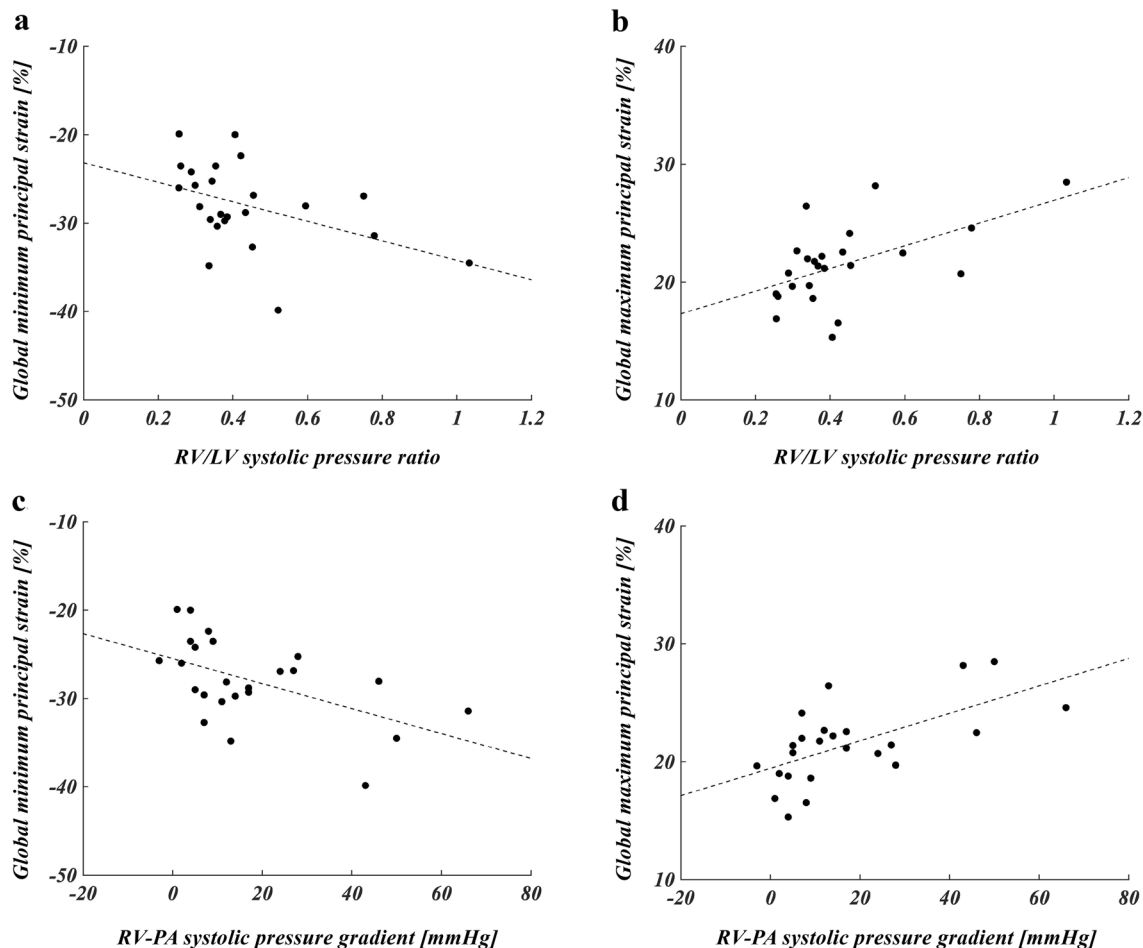


Figure 2. Correlations between global principal strains and blood pressure parameters derived from right heart catheterization. Scatter plots show the correlation of the systolic right to left ventricle (RV/LV) pressure ratio to (a) global minimum principal strain and (b) global maximum principal strain. Scatter plots show the correlation of the systolic right ventricular pulmonary artery (RV-PA) pressure gradient to the (c) global minimum principal strain and (d) global maximum principal strain.

Strain parameters	Intra-observer reproducibility				Inter-observer reproducibility			
	<i>r</i> (95% CI)	Bias (LOA)	SDD	ICC (95% CI)	<i>r</i> (95% CI)	Bias (LOA)	SDD	ICC (95% CI)
GPS _{min}	0.95 (0.81, 0.99)	-0.7% (-3.9, 2.5)	1.6	0.94 (0.78-0.98)	0.84 (0.45, 0.96)	-0.1% (-5.5, 5.4)	2.8	0.83 (0.46-0.96)
GPS _{max}	0.94 (0.75, 0.99)	0.4% (-2.1, 3.5)	1.4	0.92 (0.74-0.98)	0.85 (0.49, 0.96)	0.1% (-3.9, 4.0)	2.0	0.85 (0.52-0.96)
GCS	0.80 (0.35, 0.95)	-0.4% (-9.8, 8.9)	4.8	0.82 (0.45-0.95)	0.86 (0.49, 0.97)	0.9% (-7.5, 9.4)	4.3	0.86 (0.52-0.96)
GLS	0.89 (0.59, 0.97)	-1.2% (-6.2, 3.8)	2.6	0.88 (0.60-0.97)	0.86 (0.50, 0.97)	-1.1% (-7.0, 4.9)	3.0	0.86 (0.54-0.96)

Table 2. Reproducibility of strain measurements. *r* Pearson’s correlation coefficients, GPS_{min} global minimum principal strain, GPS_{max} global maximum principal strain, GCS global circumferential strain, GLS global longitudinal strain, LOA limit of agreement, SDD standard deviation of the difference, ICC intraclass correlation coefficient, CI confidence interval.

Cardiac catheterization. All patients with repaired TOF underwent left and right heart catheterization before PVR. Cardiac catheterization provided pressure parameters of the left ventricular, right ventricular, and pulmonary arteries.

Cine CMR imaging. Cine CMR was performed following a previous research²¹ using a 3.0T clinical scanner (Ingenia 3.0T CX; Philips Healthcare) with a dStream Torso coil using electrocardiographic gating. Steady-state

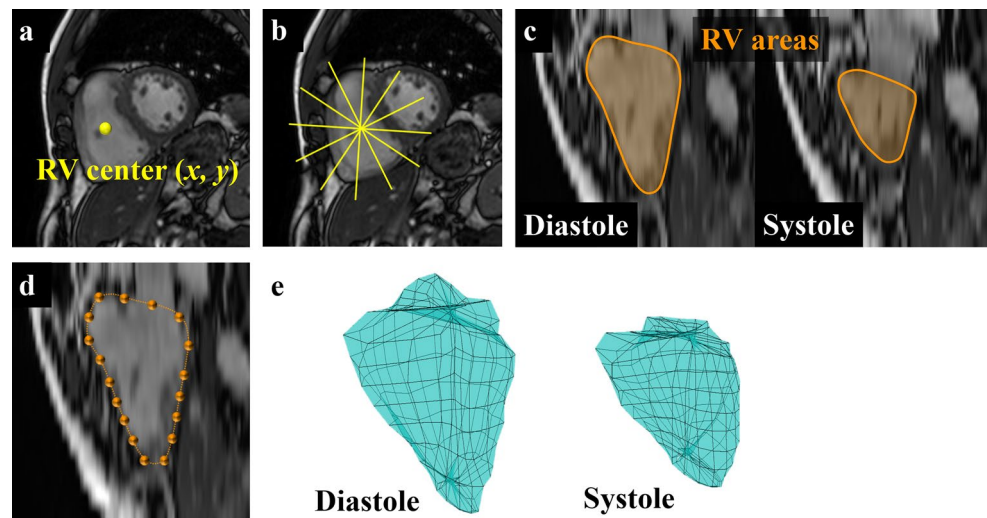


Figure 3. Segmentation of the right ventricle with radial long-axis reconstruction of short-axis cine magnetic resonance images. (a) The point (●) of right ventricular center is manually determined on the middle slice of the short-axis image in systole. (b) The images interpolated to the slice direction with the nearest-neighbor method are then automatically reconstructed into 6 radial long-axis images (—). (c) Right ventricular areas are manually segmented on radially reconstructed images at the end-diastolic and end-systolic frames. (d) Endocardial lines are automatically replaced as evenly distributed points (●). (e) Three-dimensional coordinates are automatically obtained at the end-diastolic and end-systolic frames. The right ventricular endocardial surface is individually modeled with these points in each patient.

free precession images were obtained using multi-breath holding with retrospective electrocardiogram gating in the axial and short-axis views covering the entire right ventricle with 20 phases per cardiac cycle. The axial cine imaging parameters were as follows: repetition time = 2.4 ms, echo time = 1.18 ms, SENSE factor = 2.0, flip angle = 35°, slice thickness = 8 mm, slice gap = 0 mm, field of view = 380 × 380 mm, acquisition matrix 176 × 245, and reconstruction matrix 448 × 448. The short-axis cine imaging parameters were as follows: repetition time = 2.7 ms, echo time = 1.37 ms, SENSE factor = 2.0, flip angle = 45°, slice thickness = 8 mm, slice gap = 0 mm, field of view = 380 × 435 mm, acquisition matrix 176 × 142, and reconstruction matrix 512 × 512. RV volume analysis was performed semi-automatically with subsequent manual correction using a workstation (IntelliSpace Portal, Philips Healthcare). RV volumes were measured using axial images, as previously reported²². End-diastolic volume (EDV) and end-systolic volume (ESV) were indexed to the body surface area. The ejection fraction (EF) was calculated using EDV and ESV. Stroke volume index (SV_i) was calculated as the difference between indexed EDV and ESV values (EDV_i and ESV_i, respectively). The cardiac index was the product of the SV_i and the heart rate (HR).

Strain analysis with CMR. All image processing algorithms for CMR-derived strain analyses were implemented using MATLAB R2020a (MATLAB Runtime Version 9.8; The MathWorks Inc.). Strain values were calculated from the three-dimensional coordinates of the RV endocardial point using standard short-axis cine CMR images. First, the point of the RV center was manually determined on the mid-heart short-axis slice during systole (Fig. 3a). The images interpolated to the slice direction using the nearest-neighbor method were then automatically reconstructed into six radial long-axis images at 30° around the RV point (Fig. 3b). Radial long-axis reconstructions were performed at the end-diastolic and end-systolic frames. Second, the RV areas were manually segmented on 12 images of six long-axis images with radial projection at the end-diastolic and end-systolic frames (Fig. 3c). Then, the RV endocardial lines were automatically replaced with evenly distributed points (Fig. 3d). Eighteen points were included in this study. Finally, the three-dimensional coordinates of 108 points of RV per frame (18 points for every 6 projections) were automatically obtained at the end-diastolic and end-systolic frames. The RV endocardial surface was individually modeled with these points for patient (Fig. 3e). Regional strains (ϵ), the percentages at each point, were calculated from the orthogonal lengths of circumferential, longitudinal, and radial directions at end-systole with respect to the lengths at end-diastole (Fig. 4) using Eq. (1):

$$\epsilon[\%] = \frac{(\text{systolic length} - \text{diastolic length})}{\text{diastolic length}} \times 100 \quad (1)$$

Further, the maximum and minimum PS were calculated from the three orthogonal regional strains, as per the previous research¹². In the present study, the GPS_{max} and GPS_{min} were determined as the mean values of

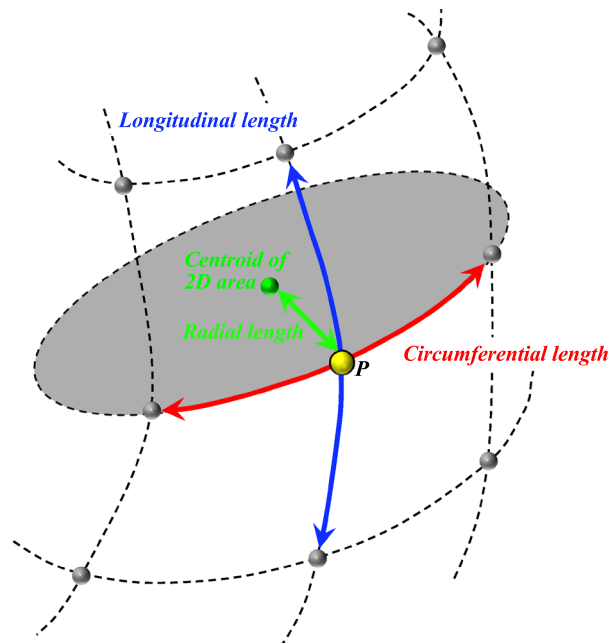


Figure 4. Strain calculations at the point of right ventricle. Regional strains at the point of right ventricular center (●) are determined as the percentage of the differences between the length at systole and diastole with respect to the length at diastole. The green point indicates the centroid of a two-dimensional area. The principal strain is calculated from three orthogonal regional strains.

maximum and minimum PS of all RV endocardial points, respectively. The GCS and GLS were the means of the strains in the circumferential and longitudinal directions for all RV endocardial points, respectively.

Statistical analysis. All statistical analyses were performed using GraphPad Prism version 8.1.2. (GraphPad Software, Inc.). Differences were considered statistically significant at $P < 0.05$. The Shapiro–Wilk test was used to evaluate the normality of the data distribution, and the mean and standard deviations were calculated. All strain parameters before and after PVR were compared using paired t-tests. One-way ANOVA with Tukey post-hoc analysis, was used for the comparisons between patient groups before and after PVR and the control group. Spearman correlation coefficients (r_s) between the GPS_{\min} and the right ventricular to left ventricular pressure (RVP/ LVP) ratio and between the GPS_{\min} and RV to pulmonary artery (PA) pressure gradient were calculated. Similarly, the r_s for GPS_{\max} were also calculated.

Intra-observer and inter-observer reproducibility. The intra-observer reproducibility of the image analysis for strain calculations was evaluated following a previous research²³. A single observer performed all analyses for 10 randomly selected patients and then blindly repeated the analyses at least 1 month later. Inter-observer reproducibility was evaluated based on the same 10 patients and performed by a second observer who was blinded to the clinical and experimental data. Pearson's correlation coefficients of intra- and inter-observer strain parameters were calculated. The intra-observer and inter-observer reproducibility of the strain measurements was evaluated using Bland–Altman analyses and intraclass correlation coefficients (ICC) with one-way or two-way random single measures (ICC [1, 1] or ICC [1, 2], respectively). The ICC values were defined as excellent (≥ 0.75), good (0.60–0.74), moderate (0.40–0.59), or poor (≤ 0.39).

Data availability

Reprints and permissions information is available.

Received: 17 June 2021; Accepted: 9 September 2021

Published online: 23 September 2021

References

1. Cuypers, J. A. *et al.* Unnatural history of tetralogy of Fallot: Prospective follow-up of 40 years after surgical correction. *Circulation* **130**, 1944–1953 (2014).
2. Geva, T., Sandweiss, B. M., Gauvreau, K., Lock, J. E. & Powell, A. J. Factors associated with impaired clinical status in long-term survivors of tetralogy of Fallot repair evaluated by magnetic resonance imaging. *J. Am. Coll. Cardiol.* **43**, 1068–1074 (2004).
3. Valente, A. M. *et al.* Contemporary predictors of death and sustained ventricular tachycardia in patients with repaired tetralogy of Fallot enrolled in the INDICATOR cohort. *Heart* **100**, 247–253 (2014).
4. Cheung, E. W., Wong, W. H. & Cheung, Y. F. Meta-analysis of pulmonary valve replacement after operative repair of tetralogy of Fallot. *Am. J. Cardiol.* **106**, 552–557 (2010).

5. Ferraz Cavalcanti, P. E. *et al.* Pulmonary valve replacement after operative repair of tetralogy of Fallot: Meta-analysis and meta-regression of 3118 patients from 48 studies. *J. Am. Coll. Cardiol.* **62**, 2227–2243 (2013).
6. Balasubramanian, S. *et al.* Impact of surgical pulmonary valve replacement on ventricular strain and synchrony in patients with repaired tetralogy of Fallot: a cardiovascular magnetic resonance feature tracking study. *J. Cardiovasc. Magn. Reson.* **20**, 37. <https://doi.org/10.1186/s12968-018-0460-0> (2018).
7. Bakos, Z. *et al.* A comparison between radial strain evaluation by speckle-tracking echocardiography and cardiac magnetic resonance imaging, for assessment of suitable segments for left ventricular lead placement in cardiac resynchronization therapy. *Europace* **16**, 1779–1786 (2014).
8. Reindl, M. *et al.* Prognostic implications of global longitudinal strain by feature-tracking cardiac magnetic resonance in ST-elevation myocardial infarction. *Circ. Cardiovasc. Imag.* **12**, e009404. <https://doi.org/10.1161/CIRCIMAGING.119.009404> (2019).
9. Mordi, I., Bezerra, H., Carrick, D. & Tzemos, N. The combined incremental prognostic value of LVEF, late gadolinium enhancement, and global circumferential strain assessed by CMR. *JACC Cardiovasc. Imag.* **8**, 540–549 (2015).
10. Haddad, F., Hunt, S. A., Rosenthal, D. N. & Murphy, D. J. Right ventricular function in cardiovascular disease, part I: Anatomy, physiology, aging, and functional assessment of the right ventricle. *Circulation* **117**, 1436–1448 (2008).
11. Ostenfeld, E. & Flachskampf, F. A. Assessment of right ventricular volumes and ejection fraction by echocardiography: From geometric approximations to realistic shapes. *Echo. Res. Pract.* **2**, R1–R11 (2015).
12. Satriano, A. *et al.* Clinical feasibility and validation of 3D principal strain analysis from cine MRI: comparison to 2D strain by MRI and 3D speckle tracking echocardiography. *Int. J. Cardiovasc. Imaging* **33**, 1979–1992 (2017).
13. Ryo, K. *et al.* Characterization of right ventricular remodeling in pulmonary hypertension associated with patient outcomes by 3-dimensional wall motion tracking echocardiography. *Circ. Cardiovasc. Imag.* **8**, e003176. <https://doi.org/10.1161/CIRCIMAGING.114.003176> (2015).
14. Sanchez-Quintana, D., Anderson, R. H. & Ho, S. Y. Ventricular myoarchitecture in tetralogy of Fallot. *Heart* **76**, 280–286 (1996).
15. Tezuka, F., Hort, W., Lange, P. E. & Nürnberg, J. H. Muscle fiber orientation in the development and regression of right ventricular hypertrophy in pigs. *Acta. Pathol. Jpn.* **40**, 402–407 (1990).
16. Greenbaum, R. A., Ho, S. Y., Gibson, D. G., Becker, A. E. & Anderson, R. H. Left ventricular fibre architecture in man. *Br. Heart J.* **45**, 248–263 (1981).
17. Satriano, A. *et al.* Characterization of right ventricular deformation in pulmonary arterial hypertension using three-dimensional principal strain analysis. *J. Am. Soc. Echocardiogr.* **32**, 385–393 (2019).
18. Sato, T., Calderon, R. J., Klas, B., Pedrizzetti, G. & Banerjee, A. Simultaneous volumetric and functional assessment of the right ventricle in hypoplastic left heart syndrome after Fontan palliation, utilizing 3-dimensional speckle-tracking echocardiography. *Circ. J.* **84**, 235–244 (2020).
19. Kawakubo, M. *et al.* Clinical usefulness of right ventricular 3D area strain in the assessment of treatment effects of balloon pulmonary angioplasty in chronic thromboembolic pulmonary hypertension: Comparison with 2D feature-tracking MRI. *Eur. Radiol.* **29**, 4583–4592 (2019).
20. Schmidt, B. *et al.* Intra- and inter-observer reproducibility of global and regional magnetic resonance feature tracking derived strain parameters of the left and right ventricle. *Eur. J. Radiol.* **89**, 97–105 (2017).
21. Yamasaki, Y. *et al.* Balloon pulmonary angioplasty improves right atrial reservoir and conduit functions in chronic thromboembolic pulmonary hypertension. *Eur. Heart. J. Cardiovasc. Imaging* **21**, 855–862 (2020).
22. Alfakih, K. *et al.* Comparison of right ventricular volume measurements between axial and short axis orientation using steady-state free precession magnetic resonance imaging. *J. Magn. Reson. Imag.* **18**, 25–32 (2003).
23. Kawakubo, M. *et al.* Feature-tracking MRI fractal analysis of right ventricular remodeling in adults with congenitally corrected transposition of the great arteries. *Radiol. Cardiothorac. Imag.* **1**, 0026. <https://doi.org/10.1148/ryct.2019190026> (2019).

Acknowledgements

This work was supported by the Center for Clinical and Translational Research of Kyushu University Hospital. The concept of this study has a pending patent (2020–181621). This work was supported by JSPS KAKENHI JP20K16729. We thank Editage (www.editage.com) for the English language editing.

Author contributions

Guarantors of integrity of entire study, M.K., Y.Y.; study concepts/study design or data acquisition or data analysis/interpretation, all authors; manuscript drafting or manuscript revision for important intellectual content, all authors; approval of final version of submitted manuscript, all authors; agrees to ensure any questions related to the work are appropriately resolved, all authors; literature research, M.K., Y.Y., D.T.; clinical studies, Y.Y., D.T., K.Y., I.S.; statistical analysis, M.K., T.M.; and manuscript editing, M.K., Y.Y., H.Y., K.I.

Competing interests

The authors declare no competing interests.

Additional information

Correspondence and requests for materials should be addressed to M.K.

Reprints and permissions information is available at www.nature.com/reprints.

Publisher's note Springer Nature remains neutral with regard to jurisdictional claims in published maps and institutional affiliations.



Open Access This article is licensed under a Creative Commons Attribution 4.0 International License, which permits use, sharing, adaptation, distribution and reproduction in any medium or format, as long as you give appropriate credit to the original author(s) and the source, provide a link to the Creative Commons licence, and indicate if changes were made. The images or other third party material in this article are included in the article's Creative Commons licence, unless indicated otherwise in a credit line to the material. If material is not included in the article's Creative Commons licence and your intended use is not permitted by statutory regulation or exceeds the permitted use, you will need to obtain permission directly from the copyright holder. To view a copy of this licence, visit <http://creativecommons.org/licenses/by/4.0/>.

© The Author(s) 2021